Electronic Wigner-molecule polymeric chains in elongated silicon quantum dots and finite-length quantum wires

Arnon Goldberg,[*] Constantine Yannouleas,[†] and Uzi Landman[‡]

School of Physics, Georgia Institute of Technology, Atlanta, Georgia 30332-0430 USA

The spectral properties of electrons confined in a wirelike quasi-one-dimensional (1D) elongated quantum dot coupler between silicon qubits are investigated with a valley-augmented unrestricted Hartree-Fock (VAUHF) method, generalized to include the valley degree of freedom treated as an isospin, allowing calculations for a large number of electrons. The lower-energy symmetry-broken solutions of the self-consistent generalized Pople-Nesbet equations exhibit, for a confinement that has been modeled after an experimentally fabricated one in silicon, the formation of Wigner-molecule polymeric (longitudinal) chains, which are initiated through charge accumulation at the edges of the finite-length quasi-1D wire. An increasing number of parallel zigzag chains form as the number of electrons loaded into the confinement is increased, with the formation of newly added chains determined by the strength of the transverse harmonic confinement. The broken-symmetry VAUHF solutions, subsequently augmented by the quantum mechanically required parity restoration, go beyond the VAUHF single-determinant solution, predicting the formation of entangled Wigner-molecule chains, the charge distributions of which obliterate the zigzag organization of the broken-symmetry solutions. The symmetry-restored VAUHF methodology enables systematic investigations of multielectron-complex nanoscale confined structures that could be targeted for future imaging-microscopy experiments in silicon and other materials (e.g., 1D domain walls in transition-metal dichalcogenide materials) and quantum information utilization.

I. INTRODUCTION

Quantum dot (QD) qubits are fundamental elements for semiconductor-based solid-state quantum computing architectures [1–3]. One of the central challenging issues in constructing scalable quantum processors is that of quantum chip large-scale integration, allowing the transfer of information between computing qubits while preserving information during transfer.

Currently, attention is focused on patterned gate-controlled elongated quantum dots (EQDs), enabling coherent transfer of spins between relatively distant quantum dot qubits [4–7], thus reducing the complexity and technical difficulties that accompany short-distance multidot couplers. To overcome the challenges of designing qubit coupling strategies, recent developments [6,7] focus on silicon-based nanodevices [1,2] guided by (i) the long coherence gained via the use of enriched ^{28}Si substrates; (ii) the successful demonstration of Si-based high-speed operation and high-fidelity-spin quantum qubits; and (iii) the vast investment made in the industry and the ensuing infrastructure availability, as well as the scientific experience already gained with Si-based technologies.

Here, we aim to gain fundamental insights into the many-body quantum nature of the electronic states in such patterned long-distance-coupling EQDs. Such an understanding is imperative for enabling theory-guided fabrication and integration of these elements into solid-state Si-based quantum information devices. Our main finding is that the extended nature of the (wirelike) EQD results in conditions where the interelectron-repulsion energy dominates over the electron quantal kinetic energy. These conditions underlie the emergent formation of pinned Wigner molecules (WMs), exhibiting a general architecture of parallel chains. Quantum WMs (manifesting sliding [8] or pinned geometrical configurations) have been predicted theoretically (see, e.g., Refs. [9–17]), and subsequently confirmed experimentally in several material systems [(Ga,Al)As single QDs [18,19], GaAs double QDs [20–22], Si QDs [23,24], carbon nanotubes [25]], and most recently, in agreement with the latest theoretical predictions [26,27], in moiré superstructures in transition-metal dichalcogenide (TMD) materials [28].

Naturally, one proceeds by formulating the many-body Hamiltonian describing the wirelike EQD, and by numerically solving the corresponding Schrödinger equation. The most accurate method to this effect is exact

---

[*]Contact author: agoldberg36@gatech.edu
[†]Contact author: Constantine.Yannouleas@physics.gatech.edu
[‡]Contact author: Uzi.Landman@physics.gatech.edu

diagonalization through the use of the full-configuration interaction (FCI) [14,16,22,24,29,30], which is limited to systems containing up to about ten confined electrons, whereas the systems of relevance for qubit couplers are expected to consist of a much larger number of electrons. Accordingly, we employ the unrestricted Hartree-Fock (UHF) [9,11,16,31], which refers to a family of self-consistent-field calculation techniques.

The UHF methodology uncovers the formation of crystallinelike space-symmetry-broken charge densities (CDs), which are finite-size analogs of the Wigner-crystal chains investigated previously theoretically in the classical limit [32] and in the context of Heisenberg chain modeling [33], as well as investigated experimentally for very long GaAs/(Al,Ga)As wires [34,35].

A proper quantum mechanical description requires the restoration [11,16,36] of the UHF broken symmetries with respect to all the symmetry operations commuting with the system Hamiltonian. Such symmetry restoration is implemented here with respect to the y-parity symmetry about the long x axis of the EQD. We discover that the parity-symmetry-restored solutions yield a substantially improved description of the CDs compared to those given by the broken-symmetry UHF solutions. Moreover, this improvement, involving an extension beyond the variational UHF single-determinant ansatz, proves to be most efficient, entailing a rather minimal computational cost for systems involving a relatively large number (dozens) of electrons.

Furthermore, the present implementation of the UHF method requires consideration of the valley degree of freedom, which is present in silicon nanostructures, treated here as a pseudospin (along the spin). This requires modifications (employed in this paper; see Sec. III) of the UHF Pople-Nesbet equations [9,11,16] formulated originally in quantum chemistry for the case of natural molecules [31]. We interchangeably refer to our calculations as UHF or valley-augmented UHF (VAUHF).

II. MANY-BODY HAMILTONIAN

We consider a squarelike slightly asymmetric confining potential along the lateral long axis (the x axis) of the EQD specified by

$$U_L(x) = \xi|x/x_0|^9\Theta(-x) + \xi(x/x_0)^{10}\Theta(x), \quad (1)$$

where $\Theta(x)$ is the Heaviside step function, $x_0 = 50$ nm, and $\xi = 0.1$ meV. This confinement corresponds to the EQD (referred to also as jellybean QD) fabricated (including the above-noted slight asymmetry) and investigated in Ref. [6]. The total confinement is given by
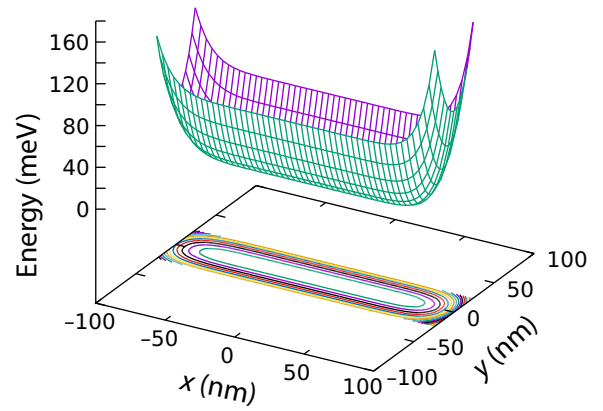
$$U(x, y) = U_L(x) + U_T(y), \quad (2)$$

FIG. 1. Illustration of the Viking-longboat-type total confining potential, $U(x,y)$, used. Square-type lateral potential, $U_L(x)$, along the x axis is given by Eq. (1). Transverse harmonic potential, $U_T(y)$, along the y direction corresponds to $\hbar\omega_y = 10$ meV and to an effective electron mass of $m^* = 0.19m_e$ (appropriate for silicon).

where $U_T(y) = m^*\omega_y^2 y^2/2$ is a harmonic potential along the transverse y direction; $m^* = 0.19m_e$ is the effective electron mass for Si and $\hbar\omega_y$ is the harmonic quantum in the transverse y direction.

An illustration of $U(x,y)$ is presented in Fig. 1. Furthermore, an illustration of the associated (single-particle) spectrum (with $\hbar\omega_y = 2.5$ meV and $m^* = 0.19m_e$) is plotted in Fig. 2.

The relevant many-body Hamiltonian is given by

$$H_{\mathrm{MB}} = \sum_{i=1}^{N}\left(\frac{\mathbf{p}_i^2}{2m^*} + U(\mathbf{r}_i)\right) + \frac{e^2}{\kappa}\sum_{i=1}^{N-1}\sum_{j>i}^{N}\frac{1}{|\mathbf{r}_i - \mathbf{r}_j|}, \quad (3)$$
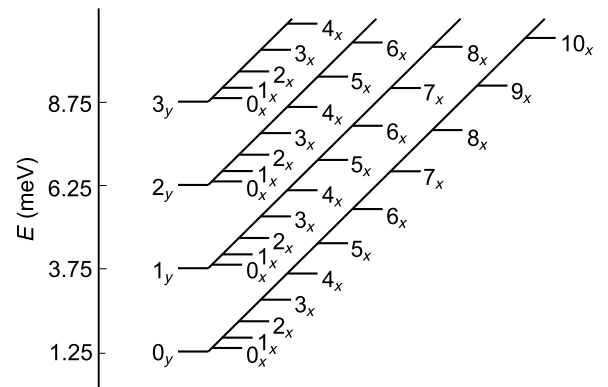
where κ is the dielectric constant.

FIG. 2. Illustration of the single-particle spectrum of electrons in the potential, $U(x,y)$, used to model the elongated QD investigated herein. For the parameters, see the text. Labels for the single-particle space orbitals are as follows: n_x, number of nodes in the x direction; n_y, number of nodes in the y direction.

III. THE VALLEY-AUGMENTED UNRESTRICTED HARTREE-FOCK FOR NANOSYSTEMS

Due to strain in Si/SiGe quantum wells and (interfacial) quantum dots (in particular, in heterostructure semiconductors) and higher subband quantization energy in metal-oxide-semiconductor devices, the energies of the (four) in-plane Si valleys are raised, resulting in two remaining degenerate valleys. Here, as is the case for the general practice for the Si QDs [1], we consider that the valley degree of freedom (VDOF) only consists of the low-energy twofold band.

As elaborated in Ref. [24], to characterize and classify the VDOF of the two remaining valleys, we consider here an isospin designation that is constructed in analogy [including the SU(2) algebra generated by the i-multiplied Pauli matrices] with that of the regular spin of the electrons (replacing $\hat{\mathbf{S}}$ with $\hat{\mathbf{V}}$ when referring to the VDOF). Obviously, in the absence of two-body interactions, the occupation of the single-particle energy states [37] in the QDs would depend on an interplay between the confinement (including an applied magnetic field) and the spin and valley effects. For the case of two-valley degeneracy (considered here), this interplay results in "quadrupling" of the spectrum (four degenerate states for each confinement state, each corresponding to a different spin and valley).

Here, we introduce the VAUHF for solving the many-body problem specified by the Hamiltonian, H_{MB}, defined in Eq. (3). Accordingly, one introduces a basis set of spatial single-particle orbitals, $\varphi_\mu(x, y)$, $\mu = 1, \ldots, K$, which are given by the K lowest-energy solutions of the auxiliary single-particle Hamiltonian:

$$H^{\mathrm{core}} = \sum_{i=1}^{N} \left(\frac{\mathbf{p}_i^2}{2m^*} + U(\mathbf{r}_i) \right). \tag{4}$$

For clarity and convenience, these solutions are sorted in ascending energy.

Subsequently, for the four families of VAUHF *spin-isospin orbitals* [38], $\psi_i^{\alpha\zeta}\alpha\zeta$, $\psi_i^{\beta\zeta}\beta\zeta$, $\psi_i^{\alpha\eta}\alpha\eta$, $\psi_i^{\beta\eta}\beta\eta$, where α (β) denotes up (down) spins, ζ (η) denotes up (down) isospins [i.e., electrons in the first (second) valley], one considers the following expansions:

$$\psi_i^{\alpha\zeta} = \sum_{\mu=1}^{K} C_{\mu i}^{\alpha\zeta} \varphi_\mu,$$

$$\psi_i^{\beta\zeta} = \sum_{\mu=1}^{K} C_{\mu i}^{\beta\zeta} \varphi_\mu,$$

$$\psi_i^{\alpha\eta} = \sum_{\mu=1}^{K} C_{\mu i}^{\alpha\eta} \varphi_\mu, \tag{5}$$

$$\psi_i^{\beta\eta} = \sum_{\mu=1}^{K} C_{\mu i}^{\beta\eta} \varphi_\mu,$$

$$i = 1, 2, \ldots, K.$$

Then, following similar steps to those reported in Chap. 3.8.2 of Ref. [31], we derive the following generalization of the Pople-Nesbet equations:

$$\sum_\nu F_{\mu\nu}^{\alpha\zeta} C_{\nu j}^{\alpha\zeta} = \varepsilon_j^{\alpha\zeta} \sum_\nu S_{\mu\nu} C_{\nu j}^{\alpha\zeta},$$

$$\sum_\nu F_{\mu\nu}^{\beta\zeta} C_{\nu j}^{\beta\zeta} = \varepsilon_j^{\beta\zeta} \sum_\nu S_{\mu\nu} C_{\nu j}^{\beta\zeta},$$

$$\sum_\nu F_{\mu\nu}^{\alpha\eta} C_{\nu j}^{\alpha\eta} = \varepsilon_j^{\alpha\eta} \sum_\nu S_{\mu\nu} C_{\nu j}^{\alpha\eta}, \tag{6}$$

$$\sum_\nu F_{\mu\nu}^{\beta\eta} C_{\nu j}^{\beta\eta} = \varepsilon_j^{\beta\eta} \sum_\nu S_{\mu\nu} C_{\nu j}^{\beta\eta},$$

$$j = 1, 2, \ldots, K.$$

with the Fock-operator matrices being given by

$$F_{\mu\nu}^{\alpha\zeta} = H_{\mu\nu}^{\mathrm{core}} + \sum_\lambda \sum_\sigma P_{\lambda\sigma}^T [(\mu\nu|\sigma\lambda) - P_{\lambda\sigma}^{\alpha\zeta}(\mu\lambda|\sigma\nu),$$

$$F_{\mu\nu}^{\beta\zeta} = H_{\mu\nu}^{\mathrm{core}} + \sum_\lambda \sum_\sigma P_{\lambda\sigma}^T [(\mu\nu|\sigma\lambda) - P_{\lambda\sigma}^{\beta\zeta}(\mu\lambda|\sigma\nu),$$

$$F_{\mu\nu}^{\alpha\eta} = H_{\mu\nu}^{\mathrm{core}} + \sum_\lambda \sum_\sigma P_{\lambda\sigma}^T [(\mu\nu|\sigma\lambda) - P_{\lambda\sigma}^{\alpha\eta}(\mu\lambda|\sigma\nu),$$

$$F_{\mu\nu}^{\beta\eta} = H_{\mu\nu}^{\mathrm{core}} + \sum_\lambda \sum_\sigma P_{\lambda\sigma}^T [(\mu\nu|\sigma\lambda) - P_{\lambda\sigma}^{\beta\eta}(\mu\lambda|\sigma\nu),$$

$$\tag{7}$$

and $\varepsilon_j^{\alpha\zeta}$, $\varepsilon_j^{\beta\zeta}$, $\varepsilon_j^{\alpha\eta}$, $\varepsilon_j^{\beta\eta}$ being the energies for the spin-isospin VAUHF orbitals. Because the φ_μs are eigenfunctions of H^{core}, one has $S_{\mu\nu} = \delta_{\mu\nu}$ for their overlaps. The two-body Coulomb matrix elements are given by

$$(\mu\nu|\sigma\lambda) = \frac{e^2}{\kappa} \int d\mathbf{r}_1 d\mathbf{r}_2 \varphi_\mu^*(\mathbf{r}_1)\varphi_\nu(\mathbf{r}_1) r_{12}^{-1} \varphi_\sigma^*(\mathbf{r}_2)\varphi_\lambda(\mathbf{r}_2), \tag{8}$$

with $r_{12}^{-1} = 1/|\mathbf{r}_1 - \mathbf{r}_2|$.

In Eq. (7), the partial density matrices are given by

$$P_{\mu\nu}^{\alpha\zeta} = \sum_a^{N^{\alpha\zeta}} C_{\mu a}^{\alpha\zeta}(C_{\nu a}^{\alpha\zeta})^*, \quad P_{\mu\nu}^{\beta\zeta} = \sum_a^{N^{\beta\zeta}} C_{\mu a}^{\beta\zeta}(C_{\nu a}^{\beta\zeta})^*,$$

$$\tag{9}$$

$$P_{\mu\nu}^{\alpha\eta} = \sum_a^{N^{\alpha\eta}} C_{\mu a}^{\alpha\eta}(C_{\nu a}^{\alpha\eta})^*, \quad P_{\mu\nu}^{\beta\eta} = \sum_a^{N^{\beta\eta}} C_{\mu a}^{\beta\eta}(C_{\nu a}^{\beta\eta})^*.$$

The total-density matrix is defined as

$$\mathbf{P}^T = \mathbf{P}^{\alpha\zeta} + \mathbf{P}^{\beta\zeta} + \mathbf{P}^{\alpha\eta} + \mathbf{P}^{\beta\eta}, \tag{10}$$

and

$$N^{\alpha\zeta} + N^{\beta\zeta} + N^{\alpha\eta} + N^{\beta\eta} = N. \tag{11}$$

The energy eigenvalues ($\varepsilon_j^{\alpha\zeta}$, $\varepsilon_j^{\beta\zeta}$, $\varepsilon_j^{\alpha\eta}$, $\varepsilon_j^{\beta\eta}$) and expansion coefficients ($C_{vj}^{\alpha\zeta}$, $C_{vj}^{\beta\zeta}$, $C_{vj}^{\alpha\eta}$, $C_{vj}^{\beta\eta}$) are obtained via self-consistent solutions of Eq. (6).

We note that, unlike the valleytronic FCI [24], the VAUHF does not conserve the total spin, $\hat{\mathbf{S}}^2$, and total valley, $\hat{\mathbf{V}}^2$, quantum numbers; it only conserves their projections S_z and V_z.

IV. VAUHF CHARGE DENSITIES

For $N = 4 - 18$ fully spin and valley polarized ($S_z = V_z = N/2$) electrons and $\hbar\omega_y = 2.5$ meV, Fig. 3 contrasts the UHF CDs at $\kappa = 11$ (silicon, top rows) to those associated with the noninteracting limit (NIL; at maximum occupation per orbital, $\kappa = 300$, and $\hbar\omega_y = 2.5$ meV, bottom rows). For all the strongly interacting electron cases, the

UHF densities exhibit explicit configurations of N well-defined humps, reflecting the formation of pinned WMs, associated with the regime of strong interelectron correlations. In contrast, the NIL CDs conform to those expected from (Aufbau) shell closures in the $U(x,y)$ confinement, with a fourfold period (due to both the spin and valley) being clearly visible for $N = 5 - 8$ [when the $(1_x, 0_y)$ orbital of the confining potential, $U(x,y)$, is sequentially occupied (see also Fig. 6); here (n_x, n_y) denotes the number of nodes in the x and y directions].

In Fig. 8 of Appendix A, we demonstrate that the CDs shown in Fig. 3 (see also Fig. 9), calculated for the spin and valley fully polarized ($S_z = V_z = N/2$) electrons, are essentially identical to the CDs for the VAUHF states with minimal spin, S_z, and isospin, V_z, projections (0 for even N or $\pm 1/2$ for odd N). This finding concurs with the magnetospectroscopy measurements [6], where it has been found that the "jellybean" quantum dot studied in these experiments lacks a visible spin structure for similar electron numbers to those investigated herein.

We recall that the strength of correlations is often expressed via the Wigner parameter [9,16], $R_W = \mathcal{E}_C/\delta$, defined as the ratio of a typical interelectron repulsive Coulombic energy, $\mathcal{E}_C$, over a typical energy gap, δ, in the
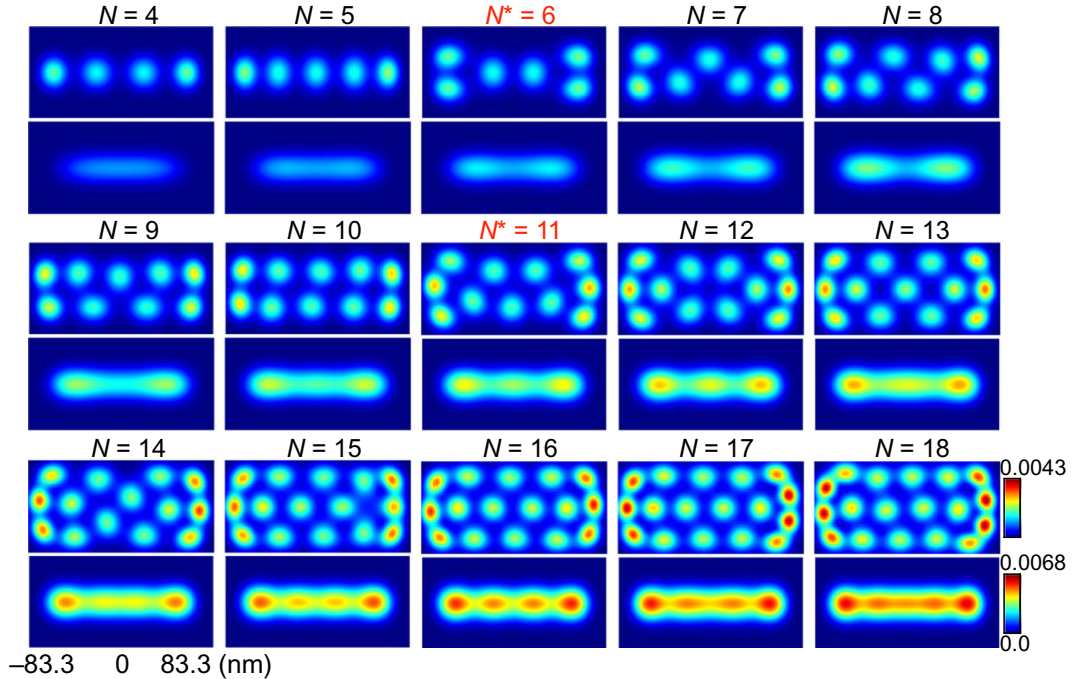

FIG. 3. UHF ground-state CDs for $N = 4 - 18$ electrons in a silicon elongated quantum dot ($\sim$110 nm long), with a transverse confinement of $\hbar\omega_y = 2.5$ meV. For each N, the CD is shown for strongly repelling electrons ($\kappa = 11$) at the top, and the CD for electrons in the noninteracting limit is shown at the bottom. Noninteracting CDs (at maximum occupation per orbital, large $\kappa = 300$, and $\hbar\omega_y = 2.5$ meV) are exhibited for all N single-row structures of a delocalized-particle nature and obey the shell-filling Aufbau rule (following spin- and isospin-exclusion rules; see text). In contrast, the strongly interacting electron CDs exhibit a transition from linear Wigner-molecule structures for $N \leq 5$ to a single zigzag chain at $N^* = 5$ and to a double zigzag chain at $N^* = 11$, which are initiated via charge accumulation occurring at the ends of the EQD. Colored bars (bottom right) indicate the charge-density scale (in units of $1/\text{nm}^2$). For details, see the text.

single-particle spectrum of $U(x,y)$; naturally, the strong-interaction regime is expected for $R_W > 1$, accompanied by WM formation. For the squarelike confinement here, we take $\mathcal{E}_C$ as the two-body matrix element of the Coulomb interaction for two electrons occupying the nodeless lowest $(0_x, 0_y)$ orbital, and for δ we take the difference between the energies of the $(0_x, 0_y)$ and $(1_x, 0_y)$ orbitals. For the EQD investigated here, we have $R_W = 23.04$ for $\kappa = 11$ and $\hbar\omega_y = 2.5$ meV, $R_W = 29.14$ for $\kappa = 11$ and $\hbar\omega_y = 10$ meV (strong interactions, case of the Si QD), and $R_W = 0.84$ for $\kappa = 300$ and $\hbar\omega_y = 2.5$ meV (noninteracting limit).

A prominent feature of the WM configurations is the successive formation, with increasing N, of complex polymeric multiple chainlike arrangements, reminiscent of the classical Wigner-crystalline chains associated with the equilibrium configurations of classical point charges [32] in infinite-length wires. Naturally, the presence of the squarelike edges here perturbs the perfect-chain formations of the infinite-length wires by forcing an accumulation of charges at the edges. The well-known zigzag configuration, however, is visible away from the edges of the EQDs for $N = 7 - 11$ (single zigzag) and $N = 14 - 18$ (double zigzag).

We note that a single row appears for $N = 1 - 5$, while a second row starts developing at $N = 7$, with $N = 6$ being a transitional stage. A third row starts developing at $N = 11$, while transitional cases towards a fourth row appear at $N = 17$ and $N = 18$, with four electrons accumulating in a line along the y direction at the edges.

Figure 4 displays the UHF CDs for fully spin and valley polarized $N = 1 - 20$ electrons for a tighter transverse confinement with $\hbar\omega_y = 10$ meV. These CDs again exhibit organization with Wigner-chain-like features; the main difference from the $\hbar\omega_y = 2.5$ meV case [see Fig. 3] is a delay in the appearance (as a function of N) of the transition regions between multiple chains. In particular, the single-chain transitions to a double zigzag chain at the region $N = 12 - 14$, with the double chain starting to form

from the edges [39]; this behavior is related to the accumulation of charge at the sharp squarelike edges of the confinement along the x direction. Notably, due to this delay, the third row does not appear in Fig. 4 in the range $N = 1 - 20$; for $\hbar\omega_y = 10$ meV, a third row is expected to develop at larger values of N.

V. RESTORATION OF PARITY ALONG THE TRANSVERSE y DIRECTION

The broken-symmetry UHF solutions violate a fundamental axiom of quantum mechanics, namely, that the single-particle CDs must preserve the symmetries of the many-body Hamiltonian. Here, we take the first step in rectifying this UHF inadequacy by restoring the parity symmetry along the transverse y direction, which is associated with a symmetric harmonic confinement, $U_T(-y) = U_T(y)$; note that the confinement along x is taken to be slightly anisotropic (in accordance with the experimentally fabricated jellybean confinement [6]).

To restore the y-parity symmetry, we apply the projection operator on the UHF Slater determinant, Ψ_{UHF}: [16,36,40]

$$\hat{\Pi} = \frac{1}{2}(1 + p\hat{\mathcal{P}}_y), \tag{12}$$

with $p = \pm 1$. $\hat{\mathcal{P}}_y$ is the many-body parity operator, which inverts the y coordinates for all electrons, namely, $\hat{\mathcal{P}}_y = \prod_{i=1}^{N} \hat{P}_y^{(i)}$, about the x axis.

The charge density associated with the projected wave function, $\Psi_{\text{PUHF}} = \hat{\Pi}\Psi_{\text{UHF}}$, is given by

$$\rho_{\text{PUHF}}(\mathbf{r}) = \mathcal{N}\langle\Psi_{\text{UHF}}|\hat{\Pi}\sum_{i=1}^{N}\delta(\mathbf{r}_i - \mathbf{r})\hat{\Pi}|\Psi_{\text{UHF}}\rangle, \tag{13}$$

where the factor $\mathcal{N}$ imposes normalization. The expansion of the symmetry-restored charge density in Eq. (13) is explicitly displayed in Eq. (C1) of Appendix C.

$N = 1$	$N = 2$	$N = 3$	$N = 4$	$N = 5$	0.0049
$N = 6$	$N = 7$	$N = 8$	$N = 9$	$N = 10$	0.0062
$N = 11$	$N^* = 12$	$N = 13$	$N = 14$	$N = 15$	0.0075
$N = 16$	$N = 17$	$N = 18$	$N = 19$	$N = 20$	0.0088

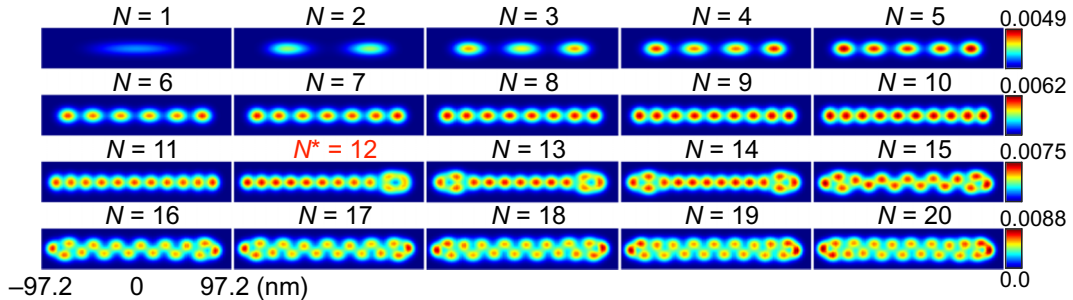−97.2   0   97.2 (nm)   0.0

FIG. 4.   UHF ground-state CDs for $N = 1 - 20$ electrons for a silicon EQD with a transverse confinement of $\hbar\omega_y = 10$ meV. $\kappa = 11$, appropriate for silicon (strong interaction). CDs exhibit a transition from one-row Wigner-molecule structures for $N \leq 11$ to a zigzag chain for $N \geq N^* = 12$, which are initiated via charge accumulation occurring at the two ends of the EQD (see $N = 12 - 14$), with the zigzag pattern fully developed for $N = 15 - 20$. For a larger number of electrons, a three-row zigzag chain structure emerges (not shown). Colored bars (on the right) indicate the charge-density scale (in units of $1/\text{nm}^2$).

The projected total energy is given by [16,36]

$$E_{\text{PUHF}} = \frac{\langle \Psi_{\text{UHF}} | H \hat{\Pi} | \Psi_{\text{UHF}} \rangle}{\langle \Psi_{\text{UHF}} | \hat{\Pi} | \Psi_{\text{UHF}} \rangle}. \tag{14}$$

Equations (13) and (14) are calculated using the property $\hat{P}_y^{(i)} Y_n(y) = \varpi_n Y_n(y)$, where $\varpi_n = (-1)^n$, $n = 0, 1, 2, \ldots$ and $Y_n(y)$ are the good-parity eigenfunctions of $U_T(y)$.

Several CD results of this parity restoration are displayed in Fig. 5; it is apparent that the zigzag motif gets obliterated by parity restoration. Whether a zigzag or a symmetry-restored CD will be the actual finding in a quasi-one-dimensional (1D) system may depend, in practice, on several additional factors, including the presence of impurities, the length of the system, and the value of the effective mass. Indeed, the longer the system, the higher the expectation of a broken-symmetry CD. Interestingly, because of the much larger mass compared to electrons, the CDs of trapped heavy ions are routinely found experimentally to exhibit broken-symmetry structures, including zigzag chains. Nevertheless, in spite of the large mass of the ions, the superposition (or entanglement) of both the "zig" and "zag" configurations is quantum mechanically allowable, and recently it has been observed experimentally [41].

Even though it is expected that (due to the much smaller electronic mass) the actual CDs of electrons in EQDs and finite-length wires would conform to those produced through the symmetry-restoration correction, a promising experimental opportunity emerged recently in the case of 1D domain walls in TMD bilayers [42], where rapid progress in STM imaging could differentiate between symmetry-broken and symmetry-preserving CDs.

VI. SECOND ENERGY DIFFERENCES

The second difference of the total energies, $\Delta_2 = E(N + 1) + E(N - 1) - 2E(N)$, corresponding to the VAUHF electronic configurations shown in Figs. 3 and 4 are shown in Fig. 6. Also shown is the noninteracting case (at maximum occupation per orbital, $\kappa = 300$, and $\hbar\omega_y = 2.5$ meV), which exhibits shell closures at $N = 4$, 8, 12, and 16, according to the Aufbau principle, with the period of 4 resulting from both the spin and valley degrees of freedom. This noninteracting behavior contrasts sharply with that of the strong-interaction cases, where polymeric WM chains are formed. We note that Δ_2 is proportional to the capacitance of the EQD.
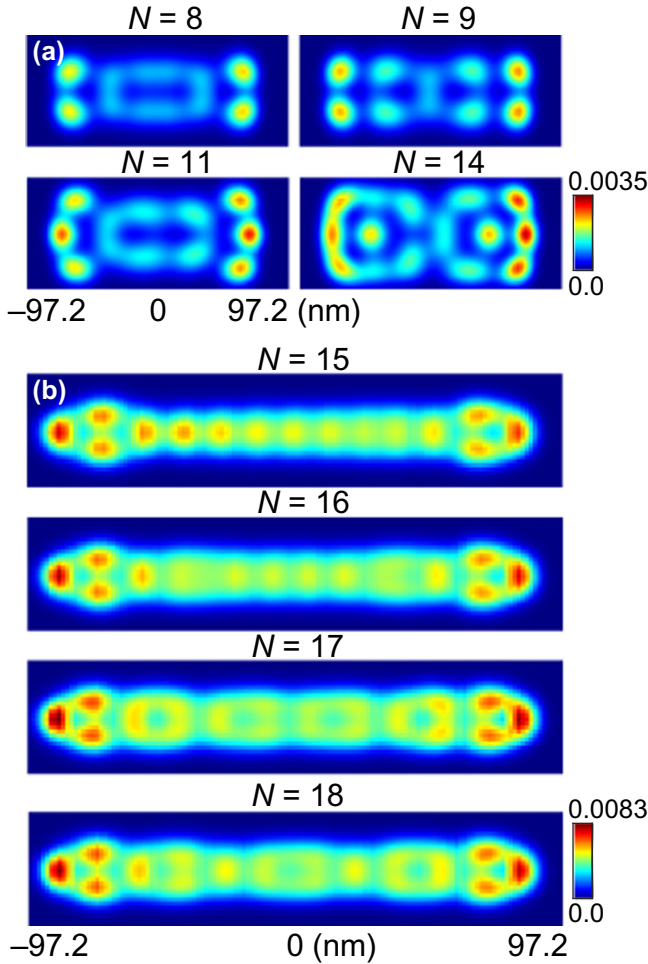

FIG. 5. Parity-restored CDs for a silicon EQD. (a) Transverse confinement of $\hbar\omega_y = 2.5$ meV. $N = 8, 9, 11, 14$ fully spin and valley polarized electrons. (b) Transverse confinement of $\hbar\omega_y = 10$ meV. $N = 15 - 18$ fully spin and valley polarized electrons. In both cases, $\kappa = 11$, which is appropriate for silicon (strong interaction). Symmetry-broken UHF CDs, corresponding to the restored ones shown in (a),(b), are given in Figs. 3 and 4, respectively. Obviously, only symmetry-broken UHF wave functions undergo symmetry restoration. CDs in units of $1/\text{nm}^2$.
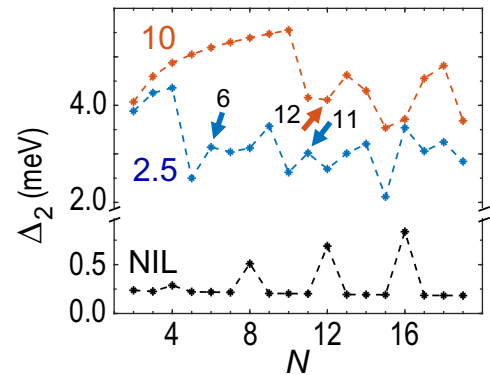

FIG. 6. UHF second energy differences, Δ_2. Curves associated with $\hbar\omega_y = 2.5$ meV and $\hbar\omega_y = 10$ meV for $\kappa = 11$ (strong interaction), as well as with the noninteracting limit (at maximum occupation per orbital, $\kappa = 300$, and $\hbar\omega_y = 2.5$ meV) are as noted. Arrows denote the transition sizes (N^*) between the multiple chains marked in Figs. 3 and 4.

VII. AN EXAMPLE OF A COMPARISON WITH FULL-CONFIGURATION INTERACTION

In Fig. 7, we present the case of a comparison between UHF and parity-restored UHF charge densities with those from the corresponding FCI [22,24] calculation. We choose the case of an elliptical external two-dimensional potential that confines $N = 4$ conduction electrons for a one-band (no valley present) semiconductor material.
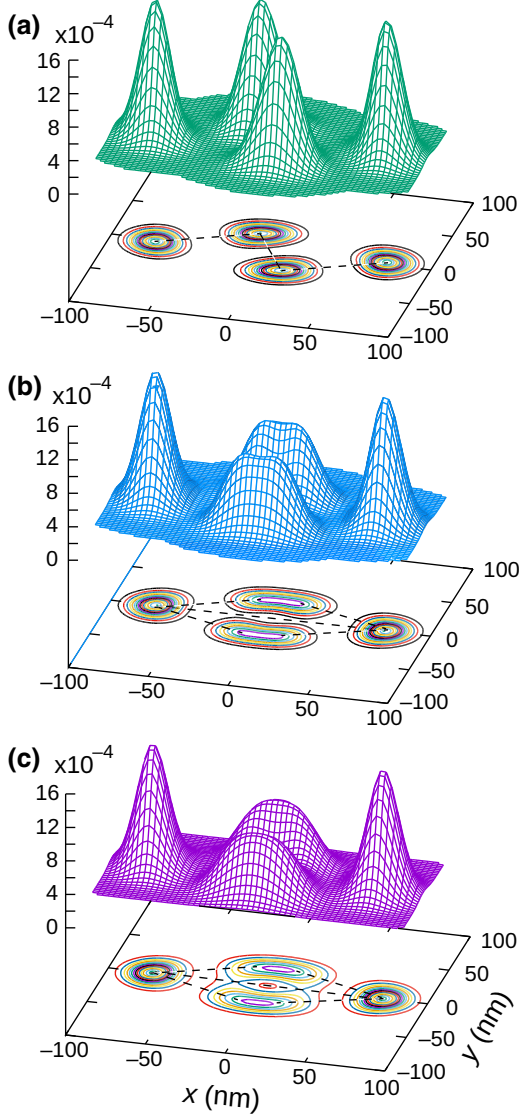

FIG. 7. Comparison of (a) symmetry-broken UHF, (b) y-parity-restored UHF, and (c) FCI CDs for the associated ground states of $N = 4$ electrons at zero magnetic field in a single elliptic quantum dot, with an effective mass of $m^* = 0.067 m_e$ and a potential confinement specified by $\hbar\omega_x = 3.00$ meV and $\hbar\omega_y = 5.64$ meV. Dielectric constant used is $\kappa = 1$. In (a),(b), $S_z = 0$. In (c), $S = S_z = 0$. Lengths in units of nm. Charge densities in units of $1/\text{nm}^2$. Charge densities are normalized to the total number of fermions, $N = 4$. Dashed lines are a guide to the eye; in (b),(c), they delineate two mirror trapezoids.

The UHF CD in Fig. 7(a) displays a broken-symmetry zigzag configuration. However, the restoration of parity along the y axis in Fig. 7(b) (which also restores x parity in this example) produces a configuration of two mirror trapezoids, which are formed by the spreading out (along the x axis) of the two middle sharp single-electron humps in Fig. 7(a). In this context, note the reduction in height of the corresponding broad humps in Fig. 7(b). The parity-restored UHF CD in Fig. 7(b) is in good agreement with the FCI CD in Fig. 7(c). Naturally, the FCI solution displays a certain degree of additional relaxation effects in the CD humps.

VIII. DISCUSSION AND CONCLUSIONS

We introduced a generalization (referred to as VAUHF) of the unrestricted Hartree-Fock methodology [9,11,16, 31] that incorporated the valley degree of freedom on an equal footing to the electronic spin. Furthermore, we explored an augmenting symmetry- (here, parity-) restoration step applied to the symmetry-broken VAUHF (going beyond the single-determinant description) that amplified and improved the quantum mechanical description of the considered nanosystem [11,16,36]. This VAUHF methodology is able to effectively and economically investigate the physics of double-quantum-dot-based Si qubits for a number of charge carriers much larger than the number accessible with FCI approaches [14,16,22,24,29,30]. The close agreement between the results of charge densities obtained via the symmetry-restored UHF methodology and those evaluated by full-configuration (exact diagonalization) computations is illustrated in Fig. 7.

A pioneering VAUHF application was presented here for the case of an elongated [7] (also referred to as a jellybean [6]) Si QD. EQDs have been proposed as long-distance couplers between solid-state qubits, thus enabling an effective solution to the problem of scalability [4–7]. Our calculations for a typical Si EQD revealed a strongly correlated regime as a particular case of Wigner molecularization [9,11,16,17], with the electrons organized in polymeric multichain arrangements, which were finite-size analogs of the infinite Wigner chains considered previously [32–35]. In this context, we note that our results agreed with the experimental findings of Ref. [7] that the charge was "well distributed" along the long lateral axis of the EQD, whereas Ref. [6] concluded that the electrons bunched together, forming several separated QDs. Instead of separated QDs, our investigations suggest that the fragmentation in the transverse direction associated with the formation of multiple chains may explain the variety of conductance behaviors reported in Ref. [6]. Conductance calculations between quantum dots coupled to the elongated coupler element, based on the many-body restored-parity VAUHF wave functions, will constitute a promising follow-up step of this work.

Finally, we note that the VAUHF findings could be further confirmed with an experimental platform associated with 1D domain walls in twisted TMD bilayers [42].

ACKNOWLEDGMENTS

APPENDIX A: SOME CASES OF CHARGE DENSITIES FOR VAUHF STATES WITH MINIMUM SPIN AND ISOSPIN POLARIZATION

In Fig. 8, we demonstrate that the VAUHF CDs shown in Fig. 3, calculated for the spin and valley fully polarized electrons, are essentially identical to the CDs for the VAUHF states with minimal spin, S_z, and isospin, V_z, projections; see the caption for specific values. This finding concurs with the magnetospectroscopy measurements [6], where it has been found that the jellybean quantum dot studied in these experiments lacks a visible spin structure for similar electron numbers to those investigated herein. To facilitate a direct comparison, in Fig. 9 we display the corresponding fully spin and isospin polarized ($S_z = V_z = N/2$) VAUHF CDs.
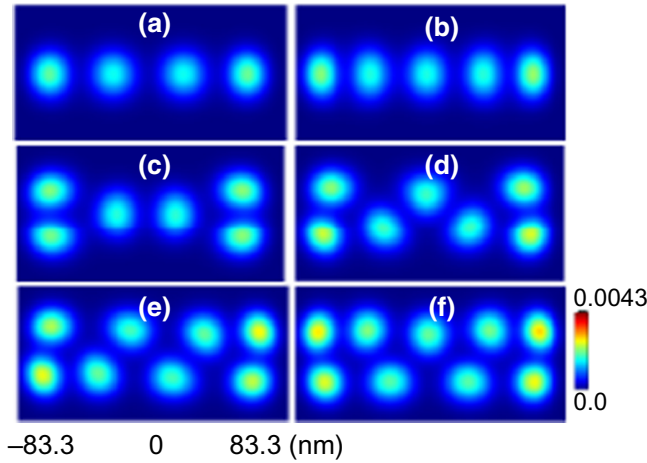

FIG. 8. Ground-state VAUHF charge densities for $N = 4 - 9$ fermions in the same elongated-dot confinement as that employed in Fig. 3 of the main text, associated with states with minimum spin and isospin polarizations, as follows: (A) $S_z = 0$, $V_z = 0$, $N = 4$. (B) $S_z = 1/2$, $V_z = 1/2$, $N = 5$. (C) $S_z = 0$, $V_z = 0$, $N = 6$. (D) $S_z = 1/2$, $V_z = -1/2$, $N = 7$. (E) $S_z = 0$, $V_z = 0$, $N = 8$. (F) $S_z = 1/2$, $V_z = 1/2$, $N = 9$. Square-like potential $U_L(x)$ along the x direction is given by Eq. (1) in the main text, with $x_0 = 50$ nm and $\xi = 0.1$ meV. Harmonic confinement $U_T(x)$ along the y direction has $\hbar\omega_y = 2.5$ meV. Other parameters used are effective mass, $m^* = 0.19 m_e$, and dielectric constant, $\kappa = 11$. Charge densities in units of $1/nm^2$.
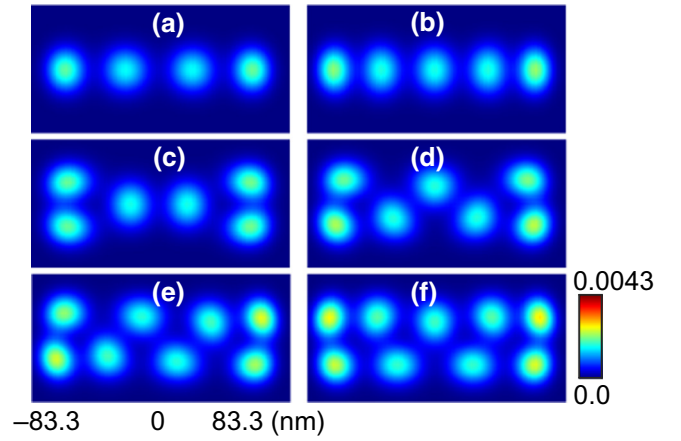

FIG. 9. Fully spin and isospin polarized ($S_z = V_z = N/2$) VAUHF CDs for $N = 4 - 9$ to be contrasted with those in Fig. 8. Parameters are the same as in the corresponding frames in Fig. 8. CDs in units of $1/nm^2$.

APPENDIX B: AN EXAMPLE OF CALCULATIONS OF PROJECTED ENERGIES

According to Eqs. (12)–(14) of the main text, there are always two projected states, Ψ_{PUHF}, with good parity eigenvalues $p = \pm 1$ for each mixed-parity state, Ψ_{UHF}. The top panel of Fig. 10 demonstrates that one of the symmetry-restored states always has an energy lower (at most equal to) than the broken-symmetry UHF state. The bottom panel of Fig. 10 displays the expectation value of the parity operator, $\langle \mathrm{UHF}|\mathcal{P}|\mathrm{UHF}\rangle$, which varies between -1 and $+1$. Notably, as a function of an increasing dielectric constant, κ, the negative-parity projected ground state is replaced by the positive-parity one, closely following the behavior of the expected value.
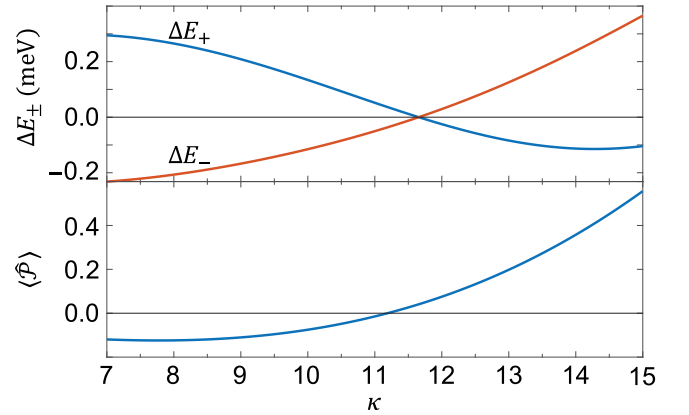

FIG. 10. Energy difference (top), $\Delta E_\pm = E_{\mathrm{PUHF}} - E_{\mathrm{UHF}}$, and expectation value of the parity operator (bottom), $\langle \mathrm{UHF}|\mathcal{P}|\mathrm{UHF}\rangle$, for $N = 7$ fully spin and valley polarized electrons as a function of the dielectric constant κ. Subscript $\pm$ corresponds to the two eigenvalues $p = \pm 1$ entering in the definition of the parity-projection operator; see Eq. (12) of the main text. Parameters used are $m^* = 0.19 m_e$ and $\hbar\omega_y = 2.5$ meV.

APPENDIX C: CLARIFICATION CONCERNING THE COMPACT EXPRESSION IN EQ. (13) OF THE MAIN TEXT

Denoting the VAUHF Slater determinant as $\Psi(x, y)$ (we drop the subscript UHF here), its mirror image about the x axis is given by $\Psi(x, -y)$, and the y-parity-restored wave function is $\propto \Psi(x, y) + p\Psi(x, -y)$, with $p = \pm 1$. Then, because the Slater determinant, $\Psi(x, -y)$, is, in general, not orthogonal to $\Psi(x, y)$, the expectation value of an operator $\mathcal{O}$ is given by

$$\frac{\langle\Psi(x,y)|\mathcal{O}|\Psi(x,y)\rangle + p\langle\Psi(x,y)|\mathcal{O}|\Psi(x,-y)\rangle + p\langle\Psi(x,-y)|\mathcal{O}|\Psi(x,y)\rangle + \langle\Psi(x,-y)|\mathcal{O}|\Psi(x,-y)\rangle}{\langle\Psi(x,y)|\Psi(x,y)\rangle + p\langle\Psi(x,y)|\Psi(x,-y)\rangle + p\langle\Psi(x,-y)|\Psi(x,y)\rangle + \langle\Psi(x,-y)|\Psi(x,-y)\rangle}. \quad \text{(C1)}$$

The operator associated with the charge density is a one-body operator, $\sum_{i=1}^{N} \delta(\mathbf{r} - \mathbf{r}_i)$.

[1] F. A. Zwanenburg, A. S. Dzurak, A. Morello, M. Y. Simmons, L. C. L. Hollenberg, G. Klimeck, S. Rogge, S. N. Coppersmith, and M. A. Eriksson, Silicon quantum electronics, Rev. Mod. Phys. **85**, 961 (2013).

[2] A. Warren and S. E. Economou, Silicon qubits move a step closer to achieving error correction, Nature **601**, 320 (2022).

[3] G. Burkard, T. D. Ladd, A. Pan, J. M. Nichol, and J. R. Petta, Semiconductor spin qubits, Rev. Mod. Phys. **95**, 025003 (2023).

[4] F. Martins, F. K. Malinowski, P. D. Nissen, S. Fallahi, G. C. Gardner, M. J. Manfra, C. M. Marcus, and F. Kuemmeth, Negative spin exchange in a multielectron quantum dot, Phys. Rev. Lett. **119**, 227701 (2017).

[5] F. K. Malinowski, F. Martins, T. B. Smith, S. D. Bartlett, A. C. Doherty, P. D. Nissen, S. Fallahi, G. C. Gardner, M. J. Manfra, C. M. Marcus, and F. Kuemmeth, Spin of a multi-electron quantum dot and its interaction with a neighboring electron, Phys. Rev. X **8**, 011045 (2018).

[6] Z. Wang, M. Feng, S. Serrano, W. Gilbert, R. C. C. Leon, T. Tanttu, P. Mai, D. Liang, J. Y. Huang, Y. Su, W. H. Lim, F. E. Hudson, C. C. Escott, A. Morello, C. H. Yang, A. S. Dzurak, A. Saraiva, and A. Laucht, Jellybean quantum dots in silicon for qubit coupling and on-chip quantum chemistry, Adv. Mater. **35**, 2208557 (2023).

[7] S. M. Patomäki, J. Williams, F. Berritta, C. Lainé, M. A. Fogarty, R. C. C. Leon, J. Jussot, S. Kubicek, A. Chatterjee, B. Govoreanu, F. Kuemmeth, J. J. L. Morton, and M. F. Gonzalez-Zalba, Elongated quantum dot as a distributed charge sensor, Phys. Rev. Appl. **21**, 054042 (2024).

[8] In the case of a confinement with circular symmetry, the WMs are referred to as rotating WMs as well.

[9] C. Yannouleas and U. Landman, Spontaneous symmetry breaking in single and molecular quantum dots, Phys. Rev. Lett. **82**, 5325 (1999).

[10] C. Yannouleas and U. Landman, Collective and independent-particle motion in two-electron artificial atoms, Phys. Rev. Lett. **85**, 1726 (2000).

[11] C. Yannouleas and U. Landman, Strongly correlated wavefunctions for artificial atoms and molecules, J. Phys.: Condens. Matter **14**, L591 (2002).

[12] A. Harju, S. Siljamäki, and R. M. Nieminen, Wigner molecules in quantum dots: A quantum Monte Carlo study, Phys. Rev. B **65**, 075309 (2002).

[13] S. A. Mikhailov, Two ground-state modifications of quantum-dot beryllium, Phys. Rev. B **66**, 153313 (2002).

[14] C. Yannouleas and U. Landman, Two-dimensional quantum dots in high magnetic fields: Rotating-electron-molecule versus composite-fermion approach, Phys. Rev. B **68**, 035326 (2003).

[15] M. B. Tavernier, E. Anisimovas, F. M. Peeters, B. Szafran, J. Adamowski, and S. Bednarek, Four-electron quantum dot in a magnetic field, Phys. Rev. B **68**, 205305 (2003).

[16] C. Yannouleas and U. Landman, Symmetry breaking and quantum correlations in finite systems: Studies of quantum dots and ultracold Bose gases and related nuclear and chemical methods, Rep. Prog. Phys. **70**, 2067 (2007).

[17] C. Yannouleas and U. Landman, Unified microscopic approach to the interplay of pinned-Wigner-solid and liquid behavior of the lowest Landau-level states in the neighborhood of $\nu = 1/3$, Phys. Rev. B **84**, 165327 (2011).

[18] C. Ellenberger, T. Ihn, C. Yannouleas, U. Landman, K. Ensslin, D. Driscoll, and A. C. Gossard, Excitation spectrum of two correlated electrons in a lateral quantum dot with negligible Zeeman splitting, Phys. Rev. Lett. **96**, 126806 (2006).

[19] T. Ihn, C. Ellenberger, K. Ensslin, C. Yannouleas, U. Landman, D. C. Driscoll, and A. C. Gossard, Quantum dots based on parabolic quantum wells: Importance of electronic correlations, Int. J. Modern Phys. B **21**, 1316 (2007).

[20] W. Jang, M.-K. Cho, H. Jang, J. Kim, J. Park, G. Kim, B. Kang, H. Jung, V. Umansky, and D. Kim, Single-shot readout of a driven hybrid qubit in a GaAs double quantum dot, Nano Lett. **21**, 4999 (2021).

[21] C. Yannouleas and U. Landman, Wigner molecules and hybrid qubits, J. Phys.: Condens. Matter (Letter) **34**, 21LT01 (2022).

[22] C. Yannouleas and U. Landman, Molecular formations and spectra due to electron correlations in three-electron hybrid double-well qubits, Phys. Rev. B **105**, 205302 (2022).

[23] J. Corrigan, J. P. Dodson, H. E. Ercan, J. C. Abadillo-Uriel, B. Thorgrimsson, T. J. Knapp, N. Holman, T. McJunkin, S. F. Neyens, E. R. MacQuarrie, R. H. Foote, L. F. Edge, M. Friesen, S. N. Coppersmith, and M. A. Eriksson, Coherent control and spectroscopy of a semiconductor quantum dot Wigner molecule, Phys. Rev. Lett. **127**, 127701 (2021).

[24] C. Yannouleas and U. Landman, Valleytronic full configuration-interaction approach: Application to the

excitation spectra of Si double-dot qubits, Phys. Rev. B **106**, 195306 (2022).

[25] S. Pecker, F. Kuemmeth, A. Secchi, M. Rontani, D. C. Ralph, P. L. McEuen, and S. Ilani, Observation and spectroscopy of a two-electron Wigner molecule in an ultraclean carbon nanotube, Nat. Phys. **9**, 576 (2013).

[26] C. Yannouleas and U. Landman, Quantum Wigner molecules in moiré materials, Phys. Rev. B **108**, L121411 (2023).

[27] C. Yannouleas and U. Landman, Wigner-molecule supercrystal in transition metal dichalcogenide moiré superlattices: Lessons from the bottom-up approach, Phys. Rev. B **109**, L121302 (2024).

[28] H. Li, Z. Xiang, A. P. Reddy, T. Devakul, R. Sailus, R. Banerjee, T. Taniguchi, K. Watanabe, S. Tongay, A. Zettl, L. Fu, M. F. Crommie, and F. Wang, Wigner molecular crystals from multi-electron moiré artificial atoms, arXiv:2312.07607.

[29] P.-O. Löwdin, Quantum theory of many-particle systems. I. Physical interpretations by means of density matrices, natural spin-orbitals, and convergence problems in the method of configurational interaction, Phys. Rev. **97**, 1474 (1955).

[30] I. Shavitt, The history and evolution of configuration interaction, Mol. Phys. **94**, 3 (1998).

[31] A. Szabo and N. S. Ostlund, *Modern Quantum Chemistry* (McGraw-Hill, New York, 1989).

[32] G. Piacente, I. V. Schweigert, J. J. Betouras, and F. M. Peeters, Generic properties of a quasi-one-dimensional classical Wigner crystal, Phys. Rev. B **69**, 045324 (2004).

[33] J. S. Meyer and K. A. Matveev, Wigner crystal physics in quantum wires, J. Phys.: Condens. Matter **21**, 023203 (2008).

[34] S.-C. Ho, H.-J. Chang, C.-H. Chang, S.-T. Lo, G. Creeth, S. Kumar, I. Farrer, D. Ritchie, J. Griffiths, G. Jones, M. Pepper, and T.-M. Chen, Imaging the zigzag Wigner crystal in confinement-tunable quantum wires, Phys. Rev. Lett. **121**, 106801 (2018).

[35] S. Kumar and M. Pepper, in *Semiconductor Nanodevices, Frontiers of Nanoscience*, Vol. 20, edited by D. A. Ritchie (Elsevier, Amsterdam, 2021), p. 7.

[36] J. A. Sheikh, J. Dobaczewski, P. Ring, L. M. Robledo, and C. Yannouleas, Symmetry restoration in mean-field approaches, J. Phys. G: Nucl. Part. Phys. **48**, 123001 (2021).

[37] These confinement-induced single-particle energy states are also referred to as "orbitals," see, e.g., the expressions "atomic orbitals," "space orbitals," and "spin orbitals" in chemistry [31].

[38] This is an apparent generalization of the term spin orbital used in chemistry and molecular physics.

[39] This behavior contrasts with that in harmonic confinements along the lateral x direction, where the zigzag chain starts forming at the center of the linear chain, a fact well known from classical calculations in the literature of trapped heavy ions; see, e.g., Refs. [43–45].

[40] F. D. Pacati and S. Boffi, Slater determinants, parity projection, and Hartree-Fock calculations, Phys. Rev. C **2**, 1205 (1970).

[41] J. Zhang, B. T. Chow, S. Ejtemaee, and P. C. Haljan, Spectroscopic characterization of the quantum linear-zigzag transition in trapped ions, npj Quantum Inf. **9**, 68 (2023).

[42] H. Li, Z. Xiang, T. Wang, M. H. Naik, W. Kim, J. Nie, S. Li, Z. Ge, Z. He, Y. Ou, R. Banerjee, T. Taniguchi, K. Watanabe, S. Tongay, A. Zettl, S. G. Louie, M. P. Zaletel, M. F. Crommie, and F. Wang, Imaging tunable Luttinger liquid systems in van der Waals heterostructures, arXiv:2404.16344.

[43] S. Ejtemaee, *Dynamics of trapped ions near the linear–zigzag structural phase transition*, PHD thesis, Simon Fraser University, 2015, available at https://summit.sfu.ca/item/16248.

[44] L. L. Yan, W. Wan, L. Chen, F. Zhou, S. J. Gong, X. Tong, and M. Feng, Exploring structural phase transitions of ion crystals, Sci. Rep. **6**, 21547 (2016).

[45] J. P. Schiffer, Phase transitions in anisotropically confined ionic crystals, Phys. Rev. Lett. **70**, 818 (1993).